

Quantum phase transitions and superconductivity in the pressurized heavy-fermion compound CeCuP₂

Erjian Cheng¹, Chuchu Zhu¹, Tianping Ying¹, Yuanji Xu², Darren C. Peets³, Jiamin Ni¹, Binglin Pan¹, Yeyu Huang¹, Linshu Wang¹, Yi-feng Yang^{2,*} and Shiyan Li^{1,4,5,*}

¹ *State Key Laboratory of Surface Physics, Department of Physics, Fudan University, Shanghai 200438, China*

² *Beijing National Laboratory for Condensed Matter Physics and Institute of Physics, Chinese Academy of Sciences, Beijing 100190, China*

³ *Ningbo Institute of Materials Technology and Engineering, Chinese Academy of Sciences, Ningbo, Zhejiang 315201, China*

⁴ *Collaborative Innovation Center of Advanced Microstructures, Nanjing 210093, China*

⁵ *Shanghai Research Center for Quantum Sciences, Shanghai 201315, China*

Corresponding author. Email: yifeng@iphy.ac.cn (Y.-F.Y.); shiyan_li@fudan.edu.cn (S.Y.L.)

Abstract

The tilted balance among competing interactions can yield a rich variety of ground states of quantum matter. In most Ce-based heavy fermion systems, this can often be qualitatively described by the famous Doniach phase diagram, owing to the competition between the Kondo screening and the Ruderman-Kittel-Kasuya-Yoshida exchange interaction. Here, we report an

unusual pressure-temperature phase diagram beyond the Doniach one in CeCuP₂. At ambient pressure, CeCuP₂ displays typical heavy-fermion behavior, albeit with a very low carrier density. With lowering temperature, it shows a crossover from a non-Fermi liquid to a Fermi liquid at around 2.4 K. But surprisingly, the Kondo coherence temperature decreases with increasing pressure, opposite to that in most Ce-based heavy fermion compounds. Upon further compression, two superconducting phases are revealed. At 48.0 GPa, the transition temperature reaches 6.1 K, the highest among all Ce-based heavy fermion superconductors. We argue for possible roles of valence tuning and fluctuations associated with its special crystal structure in addition to the hybridization effect. These unusual phase diagrams suggest that CeCuP₂ is a novel platform for studying the rich heavy fermions physics beyond the conventional Doniach paradigm.

Introduction

As prototype examples of strongly correlated electron systems, heavy-fermion (HF) compounds have been intensively investigated due to their various fascinating properties¹⁻⁴. They are mostly rare earth or actinide (Ce, Yb, U, etc.) intermetallics with partially filled $4f$ or $5f$ orbitals¹⁻⁶. The f -electrons are often localized, in particular in Ce-based compounds, and coupled with conduction electrons through a local antiferromagnetic exchange interaction. The resulting Kondo screening effect competes with the induced long-range Ruderman-Kittel-Kasuya-Yoshida (RKKY) interaction between f -moments, causing a quantum phase transition between magnetically ordered states and a disordered heavy Fermi liquid state under external tuning such as the pressure, doping or magnetic field^{3,7}. This is qualitatively described by the famous Doniach phase diagram⁷, as schematically

shown in the inset of Fig. 1(b). In most Ce-based HF compounds, the Doniach paradigm has been extensively examined, with only few possible exceptions³.

In proximity to the magnetic quantum critical point (QCP), superconductivity often emerges, mostly ascribed to the spin-fluctuation-mediated pairing mechanism, and shares some common features with other unconventional superconductors such as the cuprate, iron-based and organic superconductors^{3,4}. Other pairing mechanisms such as valence or orbital fluctuations have also been proposed, but no concrete evidences have been established⁸⁻¹¹. A unified explanation is still lacking and the role of quantum criticality in driving superconductivity is not yet fully understood. Seeking new materials with potentially different low-energy quantum fluctuations and pairing mechanisms may shed light on this long-standing issue.

In this work, we report systematic magnetic susceptibility, specific heat and electrical transport measurements of the heavy-fermion compound CeCuP₂. Our results are summarized in the P - T phase diagrams of Figs. 1(a) and (b). At ambient pressure, CeCuP₂ exhibits typical NFL behavior featuring a quasi-linear temperature-dependent resistivity and divergent specific heat and magnetic susceptibility above 2.4 K. Around 2.4 K, a crossover turns the system into a FL state at low temperatures. Scaling analyses of the magnetic susceptibility and Grüneisen ratio confirm the quantum critical behavior at ambient pressure and zero magnetic field. Under pressure, electrical transport measurements identify multiple quantum phase transitions. For pressure $P < P_{c1} \sim 0.7$ GPa, the system always turns into a metallic Kondo coherent state with lowering temperature. But in contrast to most Ce-based HF compounds, the coherence temperature T_{coh} is gradually suppressed with increasing pressure and diminishes at P_{c1} , where the insulating-like Kondo incoherent state persists down to our lowest measured temperature of 0.3 K. For $P_{c1} < P < P_{c2} \sim 4.0$ GPa, the

incoherent state is gradually weakened. A second metallic state takes over at low temperatures above P_{c2} , accompanied by the first superconducting transition. The T_c s for the first superconducting state (SC1) display a clear dome shape with a maximum transition temperature of 4.3 K at 7.8 GPa. At $P_{c3} \sim 11.0$ GPa, the first superconducting state disappears. With further pressurization beyond P_{c3} , the second superconducting state (SC2) arises, and spans over a wide pressure range, which is much broader in pressure than that in usual HF superconductors³. The T_c for SC2 exhibits a dip at $P_{c4} \sim 34.0$ GPa, and then goes up again. At 48.0 GPa, T_c reaches 6.1 K, the highest among all Ce-based heavy fermion superconductors³. The overall phase diagram is shown in Figs. 1(a) and (b) and looks strikingly different from the usual Doniach one, which suggests that other essential factors such as the valence change of Ce-ions should be considered for understanding CeCuP₂.

Results

Non-Fermi liquid behavior and anomalous crossover transition. The growth of CeCuP₂ was first reported by Chykhrij *et al.*¹² with the space group $I4/mmm$ (139) and the Ce : Cu : P stoichiometric ratio of 1 : 1.09 : 1.8. Each unit cell has one Wyckoff position (4e) for Cerium atoms located between neighboring layers and forming a tetragonal structure. Copper atoms are distributed on two different Wyckoff positions denoted as Cu1 and Cu2, with Cu1 (4d) atoms forming a 12-vertex polyhedron. Phosphorus atoms occupy three Wyckoff positions denoted as P1, P2 and P3. The P1 (4e) and Cu2 (4e) atoms form Platonic solids, and the P2 (4c) and P3 (8j) atoms have distorted cubic co-ordinations. The crystal structure is displayed in the inset of Fig. 1(a). According to the ICSD data (No. 83894) of CeCu_{1.09}P_{1.87} built on Chykhrij's work¹², we found fractional occupancies on Cu2, P2, and P3, which explain the non-integral stoichiometric ratio. To determine the accurate chemical

composition and crystallographic parameters of our crystals, we have conducted the inductively coupled plasma (ICP) spectroscopy and the Rietveld refinement of powder X-ray diffraction (XRD) studies. Detailed results and discussions can be found in the Supplementary Information (Supplementary Note 1)¹³, yielding the Ce : Cu : P ratio of 1 : 1.14 : 2 for our samples. For simplification, we still use CeCuP₂ throughout this work.

Single crystals of CeCuP₂ were grown from molten Sn flux and demonstrated by XRD measurements (see Supplementary Fig. 1)¹³. Figure 2(a) displays the in-plane resistivity from 0.3 to 4 K at zero magnetic field and shows three distinct regimes. Below ~ 1.5 K, the data follows exactly the Fermi liquid power law, $\rho(T) = \rho_0 + AT^n$ with $n = 2$, where ρ_0 is the residual resistivity and A the electronic scattering coefficient. Our best fit gives $\rho_0 = 0.058$ m Ω cm and $A = 0.0048$ m Ω cm K⁻². Above 2.4 K, the resistivity exhibits linear temperature dependence, typical of NFL behavior. In between, there is an abrupt crossover from the NFL to FL states. At higher temperatures as shown in the inset of Fig. 2(a), CeCuP₂ behaves like a typical heavy fermion metal, with a resistivity maximum at $T_{\text{coh}} \sim 20.5$ K marking the transition from a metallic Kondo coherent state to a high-temperature insulating-like Kondo incoherent state. For contrast, the resistivity of LaCuP₂ (see Supplementary Fig. 2) is also displayed in the Supplementary Information¹³.

To clarify the NFL-to-FL crossover around 2.4 K, we have conducted the specific heat measurements. Figure 2(b) shows the specific heats of CeCuP₂, LaCuP₂, and the magnetic contributions (C_m/T) extracted by comparison against that of the nonmagnetic analogue LaCuP₂ from CeCuP₂. Herein, we presume that the electron and phonon contributions in LaCuP₂ are identical to those in CeCuP₂, which is less rigorous due to the special crystal structure. We note that the specific heat in CeCuP₂ and LaCuP₂ shows similar behavior above the coherence temperature, and in

particular both have peaks around $T \sim 100$ K. The specific heat of CeCuP_2 is larger than that of LaCuP_2 over the entire measured range, and this enhancement may stem from the integrated effects of the f -electron excitations, the hybridization between the conduction electrons and the excited crystalline electric field (CEF) doublets, and the sample quality. The solid curve in Fig. 2(b) represents the magnetic entropy S_m calculated from C_m/T . The effective Kondo temperature (T_K), estimated from $S_m(T_K) = 0.65 R \ln 2$ ¹⁴, is about 9.5 K. S_m reaches $0.38 R \ln 2$ at the low-temperature hump and the remaining entropy of the Kramers doublet is gradually released till 29 K somewhat above T_{coh} . The green points in Fig. 2(b) shows the resulting C_m/T of CeCuP_2 at zero field, which is seen to diverge logarithmically below 10 K but interrupted by a hump at ~ 1.8 K. The hump causes a departure from the logarithmic divergence below 2.4 K (marked as T^*). This is in exact correspondence with the NFL-to-FL crossover in the resistivity. The hump cannot be described by a two-level Schottky function (Supplementary Fig. 3(a))¹³, excluding the possibility of a Schottky anomaly indirectly. The shape of the hump also does not follow a distinct first-order ' λ '-anomaly or a jump characteristic of a second-order phase transition; therefore, it likely cannot be attributed to a long-range magnetic order. A similar feature has also been found in the arsenic analogue CeCuAs_2 around 4 K, where it has been explained as a disorder-driven continuous metal-insulator transition resulting in a gradual loss of density of states (DOS) with decreasing temperature, although the low-temperature downturn in C/T in CeCuAs_2 is still not well understood^{15,16}.

The absence of long-range magnetic order is more clearly demonstrated in Fig. 2(c), where the temperature dependence of the magnetic susceptibility is plotted down to 1.8 K, and below 2 K (left inset) measured in a ^3He cryostat. Short-range magnetic order is also excluded by field cooling (FC) and zero FC (ZFC) (Fig. S4(a)), and *ac* magnetic susceptibility measurements (Supplementary Fig.

4(b))¹³. In CeCuAs₂, spin-glass freezing and Schottky anomaly origin behind the low-temperature hump in specific heat have also been excluded¹⁴, as we did for CeCuP₂. The right inset gives the inverse susceptibility at 0.5 T. By fitting the linear part of the data with the Curie-Weiss law, $\chi = C/(T-\theta)$, we obtain $\theta \sim -284$ K and an effective magnetic moment (μ_{eff}) of $1.44 \mu_{\text{B}}$. The former indicates an effective antiferromagnetic exchange interaction between f -moments, but the size of the moment is significantly reduced compared to the expected value of $2.54 \mu_{\text{B}}$ for a free Ce³⁺ ion, suggesting possible mixed-valence of the Ce ions in CeCuP₂. Interestingly, the magnetic susceptibility at 0.05 T exhibits an evident power-law divergence with $T^{-0.71}$ at low temperatures. A comparable exponent has been observed previously in YbRh₂(Si_{0.95}Ge_{0.05})₂ with $T^{-(0.6 \pm 0.1)}$ and explained in terms of local quantum criticality¹⁷. The similarity suggests potential magnetic quantum-critical fluctuations in CeCuP₂ at ambient pressure.

More insight on the NFL-to-FL crossover can be obtained from the Hall measurements (Supplementary Fig. 5)¹³. Figure 2(d) shows the temperature-dependent Hall coefficient (R_H) obtained by fitting the Hall resistivity from 0 to 3 T. We found dominant electron carriers from 0.3 to 20 K. With lowering temperature to 4 K, the magnitude of R_H increases monotonously, indicating the increase of concentration of electron carriers. Upon decreasing the temperature to ~ 2.4 K, a peak in R_H emerges, and then R_H decreases. The peak observed in R_H may arise from phase transitions smeared by disorders. Since magnetic ordering has been excluded in our experiments, the peak in R_H possibly comes from structural variations in consideration of the fractional occupancies on Cu2, P2 and P3^{18,19}. At the lowest measured temperature, the density of electrons can be estimated to be about $0.006 e^-$ per formula unit, ten times smaller than that in usual HF metals such as CeCoIn₅. According to Nozières' argument^{20,21}, this may produce a protracted Kondo screening

^{22,23}, as the f -moments cannot be fully screened. In CeCuP₂, we anticipate that the special electronic structures of the fractionally occupied Cu2, P2, and P3 atoms may tune the Fermi level and leave only few carriers in the conduction bands. Thus, CeCuP₂ provides a unique platform for valence tuning in HF materials. The NFL-to-FL anomalies may be associated with this special property of CeCuP₂, an interesting topic to be investigated using the state-of-the-art angle-resolved photoemission spectroscopy (ARPES) or scanning tunneling microscopy (STM) in the future.

The above anomalous features are also reflected in the field measurements. Figure 3(a) plots the in-plane resistivity as a function of the magnetic field applied along the c axis. All resistivity curves cross roughly at a single point at ~ 2.4 K, around which the magnetoresistance (MR) changes sign. This coincides with the abrupt change in the carrier concentration. The crossing point shifts slightly to higher temperature with increasing field. Isothermal MR measurements (Supplementary Fig. 6(a)) demonstrate the evolution of the MR ¹³. In Fig. 3(b), the hump in the field-dependent specific heat also shifts gradually to higher temperatures, as observed in CeCuAs₂ ¹⁵. The overall suppression of the specific heat indicates the suppression of quasi-particle excitations with increasing field ¹³.

The field measurements provide crucial information on the QCP in CeCuP₂ at ambient pressure. To investigate the origin of the NFL above 2.4 K, we measured the magnetic susceptibility under high fields (see Supplementary Fig. 4(c)). In many HF systems, the critical scaling may be described within a fermion-condensed picture ²⁴⁻²⁶. Motivated by the established scaling method ^{25,26}, we identify a scaling of its free energy in the scaling variable $x = T^*(B) \sim B^{0.4}$. The exponent of B is acquired by fitting the maximum value of $-d\chi/dT$ in different fields. Its value of 0.4 is smaller than in other QC systems, for example, 1 in β -YbAlB₄ ²³, 0.59 in YFe₂Al₁₀ ²⁶, and 1.05 in CeNi₂Ge₂ ²⁷. As shown in Fig. 3(c), the magnetic susceptibility in different fields shows a remarkable scaling collapse

for $1.8 \text{ K} \leq T \leq 18 \text{ K}$ and $B \leq 7 \text{ T}$, extending over about three orders of magnitude in the scaling variable x , where $\frac{-d\chi}{dT} B^{0.71} = \Psi\left(\frac{T}{B^{0.4}}\right)$. This scaling behavior reveals an important property of the underlying free energy. Inspired by the scaling functions $f_{\text{F}}(x)$ that were found in $\beta\text{-YbAlB}_4$ ²⁵ and $\text{YFe}_2\text{Al}_{10}$ ²⁶, we propose a similar expression for CeCuP_2 — $M = B^{1-\varepsilon+y} f_{\text{M}}(x)$ with $f_{\text{M}}(x) = c(x^\alpha + a^2)^{\frac{-\varepsilon}{2}}$ and $x = T/B^y$. The scaling function f_{M} is related to the original scaling function of the free energy f_{F} , as described in Ref. 26, and y is a magnetic field tuning parameter. By taking the temperature derivative of $\chi = M/B$, we deduce the scaling equation $\frac{-d\chi}{dT} B^\varepsilon = \frac{ca\varepsilon}{2} x^{\alpha-1} (x^\alpha + a^2)^{\frac{-\varepsilon}{2}-1}$. Here, c , a , α and ε are the fitting parameters. In the limit of a field-driven FL phase ($x \ll 1$), the parameter α is 2^{25,26}. As shown in Fig. 3(c), the scaling equation can fit the data very well in the limit of quantum criticality ($x \gg 1$) with $\alpha = 2$, but fails in the limit of the field-driven FL phase it would be expected to describe. The reason for this failure may be ascribed to which the system is in the mixed-valence state under ambient pressure. The parameters c , a and ε from the fit with $\alpha = 2$ are 0.026 ± 0.001 , 1.842 ± 0.005 , and 0.75 ± 0.05 , respectively. The parameter $\varepsilon = 0.71$ can be determined experimentally (see Fig. 2(c)), thus the data agrees well with each other within the fitting uncertainty. We can also treat α as a free parameter to fit the data for all x , yielding an excellent fit. The parameters of c , a , α and ε in this case are 0.024 ± 0.001 , 2.743 ± 0.003 , 2.80 ± 0.01 , and 0.6 ± 0.1 , respectively, and ε is again consistent with the experimental value. In contrast to the exponent of x , the parameter $\alpha = 2.8$ is significantly larger than that expected for a FL phase. To explain this, more theoretical efforts will be required.

A $T^{-2.00(2)}$ divergence is also found in the Grüneisen ratio divided by the magnetic field, as shown in the inset to Fig. 3(c). This observation implies further critical behavior^{25,26}, although the validity of establishing the QCPs through the Grüneisen ratio is still under debate²⁸. Putting together, all

evidence supports quantum criticality possibly interrupted by the NFL-to-FL crossover at zero field and ambient pressure in CeCuP₂. We have also checked the field dependence of the resistivity coefficient A and the upper boundary of the Fermi liquid regime T_0 . As shown in Fig. 3(d), T_0 changes slightly from 1.7 to 1.5 and A also decreases, suggesting reduced electronic scatterings.

Pressure-induced quantum phase transitions and superconductivity. Next, we turn to pressure measurements. Due to the low magnitude of the energy scales in HF materials, pressure is an efficient tool to tune the ground state properties. Figures 4(a) and 4(b) show the resistivity under pressure up to 2.16 GPa measured from 2 to 300 K in PPMS and from 0.3 to 5 K using a ³He refrigerator, respectively. With increasing pressure up to $P_{c1} \sim 0.7$ GPa, T_{coh} is gradually suppressed to zero and the magnitude of the resistivity below T_{coh} increases correspondingly. The resistivity exhibits semi-metallic behavior at 0.71 GPa (left panel of Fig. 4(b)) and its value at 0.3 K is about 22 times larger than that at ambient pressure. The inset of Fig. S7 summarizes the evolution of T_{coh} and the resistivity at 0.3 K with increasing pressure¹³. It is well-known that T_{coh} marks the emergence of heavy quasiparticles and its magnitude reflects the effective strength of collective hybridization between f and conduction electrons^{29,30}. The decrease of T_{coh} in CeCuP₂ is in sharp contrast to most Ce-based HF materials, where pressure usually enhances the hybridization. In the Doniach paradigm, this is caused by the increase of the Kondo coupling $|J|$, namely $\partial|J|/\partial P > 0$ ^{30,31}. The situation in CeCuP₂ is therefore highly unusual. Similar suppression has also been observed in CeRhIn₅ below 1.2 GPa³¹, but ascribed to other effects such as the spin freezing or enhanced 2D AFM fluctuations associated with its low-temperature AFM order³¹, and UTe₂³², the increase in valence towards a U⁴⁺ (5f²) state, which is generally expected to drive the system from superconducting to

antiferromagnetic³². In Yb-based HF compounds, T_{coh} also decreases with pressure due to the shift of the f levels away from the Fermi energy, which, would typically lead to magnetic ordering at high pressure. Regardless of Ce-based, U-based or Yb-based, the reduced coherence temperature is proposed to be related to magnetic fluctuations. Therefore, the decrease in the Kondo coherence temperature in CeCuP₂ motivates us to check the magnetic field effect under pressure. Supplementary Figure 6(b) shows the pressure dependence of the MR investigated at 2 K (detail discussions can be found in the Supplementary Note 7¹³), finding the change of the scattering mechanism, indicative of the possible magnetic fluctuations, although there is no any indication for magnetic transitions in resistivity under pressure (Figs. 4(a) and 4(b)). In Supplementary Fig. 10, we demonstrate the existence of pressure-induced valence fluctuations of Ce 4f electrons in CeCuP₂ by means of the scaling of resistivity under pressure. As a result, the decrease of coherence temperature and the change of MR under pressure are maybe related to the pressure-induced fluctuations of the Ce 4f electrons in CeCuP₂. To confirm this proposal, more works are expected to investigate the magnetic behavior under pressure in the future.

The critical behavior around P_{c1} is also different. For a pressure-induced magnetic QCP, the electronic scattering coefficient A usually diverges in the vicinity of the QCP³, but this is not observed in CeCuP₂. Rather, we found a moderate enhancement near P_{c1} (Supplementary Fig. 7)¹³. This suggests that the coherent-to-incoherent transition at P_{c1} is not associated with a usual magnetic or delocalization transition often observed in other HF compounds. Upon further increasing pressure up to $P_{c2} \sim 4.0$ GPa, the resistivity becomes suppressed but the system remains in an incoherent state down to the lowest measured temperature. In this intermediate region, the resistivity responds very differently to the magnetic field compared to the low-pressure region. Fig. 4(c) shows the resistivity

at 2.16 GPa, which decreases monotonically with increasing field, indicating a change in the scattering mechanism. Thus, the phase diagram of CeCuP₂ cannot be simply understood within the Doniach paradigm based on the competition between long-range magnetism and Kondo hybridization. It is essential to take other important factors into consideration, for example, charge fluctuations.

HF superconductivity has often been observed in the vicinity of magnetic or valence instabilities³. Inspired by this, we have carried out further pressure measurements on CeCuP₂ polycrystal obtained by crushing a single crystal. Figure 4(d) plots the temperature dependence of the normalized resistance at different pressures without pressure transmitting medium (denoted as Run1). The Kondo incoherent phase persists up to 4.6 GPa, above which a small drop in the resistance is seen to emerge at low temperatures. At 6.3 GPa, the resistance starts to display typical metallic behavior. Surprisingly, a superconducting drop emerges around the same pressure. The superconducting temperature (T_c^{onset}) defined by the onset of the transition reaches 4.7 K at 14.8 GPa, as shown in the inset. To verify the superconductivity observed in CeCuP₂, pressure experiments were repeated in another device with NaCl as the pressure transmitting medium (denoted as Run2), as displayed in Fig. 4(e). A small drop in the resistance emerges at 4.0 GPa. With increasing pressure to 7.8 GPa, T_c increases to a maximum of 4.3 K, and then decreases beyond 7.8 GPa. At 11.0 GPa and down to 1.9 K the lowest temperature we measured, there is no any indications of superconductivity. The pressure-dependent T_c ranging from 4.0 to 11.0 GPa displays a clear dome shape, as plotted in Fig. 1(b).

Upon further compression beyond 11.0 GPa, the second superconducting state (SC2) arises, it spans over a wide pressure range, which is much broader in pressure than that in usual HF

superconductors³. At ~ 34.0 GPa, the T_c displays a dip, which is a mystery for now. At 48.0 GPa the highest pressure we measured, T_c reaches 6.1 K³. To verify the superconducting transition and obtain the upper critical fields ($\mu_0 H_{c2}$ s), we applied the magnetic field at several pressures. As shown in Supplementary Fig. 9, the transition is gradually suppressed by magnetic field, as expected for superconductivity, although zero resistance hasn't been achieved. Considering the fractional occupancies of the crystal sites in CeCuP₂, we propose several scenarios for the nonzero resistance. The first one is the poor grain contact in the polycrystalline sample and an anisotropic superconducting order parameter³³. A single crystal high-pressure transport study may thus help to find zero resistance, and an even higher transition temperature in the superconducting phases of CeCuP₂. The second is that the actual stoichiometric ratio of Ce : Cu : P = 1 : 1.14 : 2 is not optimal for superconductivity. The crystal structure of CeCuP₂ provides a unique platform for chemical doping. Therefore, tuning the concentration of copper and phosphorus may facilitate the observation of zero resistance. The third is the local inhomogeneity under pressure, which would be associated with a spatial variation of the copper and phosphorus concentration, local density of states, and superconducting order parameter³⁴. This inhomogeneity would lead to filamentary superconductivity³⁴. The last one is that the pressure is inhomogeneous and not locally hydrostatic. This could drastically smear out the transition, especially if the order parameter is anisotropic and especially at higher pressures. Determining the reason for nonzero resistance is left for a future study. Previously, the highest transition temperatures reported among all Ce-based HF superconductors are 2.3 K for CeCoIn₅ at ambient pressure³⁵ and 2.5 K for CeAu₂Si₂ at ~ 22.5 GPa⁹. Our observed transition temperature in CeCuP₂ is the new highest record among all Ce-based HF superconductors.

To understand the pairing mechanism, we plot in Fig. 4(f) the temperature dependence of $\mu_0 H_{c2}$

and use the Ginzburg-Landau (GL) formula $\mu_0 H_{c2}(T) = \mu_0 H_{c2}(0)(1-(T/T_c)^2)/(1+(T/T_c)^2)$ to fit the data. The values are estimated to be 0.050(6) T, 0.0192(9) T, 0.40(2) T, 0.37(2) T, 1.85(5) T and 2.07(7) T for 8.4 GPa, 9.7 GPa, 15.4 GPa, T_c^{onset} at 23.3 GPa, $T_c^{10\%}$ at 23.3 GPa (denoted as 23.3 'GPa) and 42.5 GPa, respectively, which are much lower than the Pauli limiting fields $H_P(0) = 1.84T_c \sim 7.9, 6.9, 7.7, 8.0, 5.9$ and 10.3 T, respectively, indicating that Pauli pair breaking is not relevant^{36,37}. To get some insight into the superconducting pairing, the initial slopes of the upper critical field at 8.4, 9.7, 15.4, 23.3 and 42.5 GPa have been calculated, yielding -0.012, -0.005, -0.096, -0.428 and -0.372 T/K, respectively. The magnitudes of the initial slopes are much smaller than in other heavy-fermion superconductors³, suggestive of conventional superconducting pairing. However, this quantity can be affected by other factors, such as disorder, so a small initial slope of the upper critical field cannot serve as a smoking gun for the conventional superconducting pairing. For HF superconductors, a $\mu_0 H_{c2}$ not exceeding $H_P(0)$ can be also found in other Ce-based systems, for example, CeRh₂Si₂³⁸, CePd₂Si₂³⁹, Ce₃PtIn₁₁⁴⁰. To better show the $\mu_0 H_{c2}$ behavior of CeCuP₂ among Ce-based HF superconductors, we list the ratio of $\mu_0 H_{c2}(0)$ to $H_P(0)$, as displayed in Supplementary Fig. 9. For CeRh₂Si₂, the resistivity decreases below 0.5 K at ~ 1.05 GPa, and the $\mu_0 H_{c2}$ is estimated to be 0.28 T, less than 0.92 T calculated from the Pauli rule³⁸. Therefore, the low $\mu_0 H_{c2}$ s in CeCuP₂ could not exclude the possibility of unconventional superconducting pairing completely, although the possibility of BCS-like origin cannot be ruled out either. We also note that the low value of upper critical field in CeCuP₂ may suggest flux pinning at grain boundaries. In spite of this, two separated superconducting phases observed in CeCuP₂ are quite unconventional^{3,41,42}.

Often, superconductivity near an AFM QCP as in CeCoIn₅ may be ascribed to a spin-fluctuation-mediated pairing mechanism³. In CeCuP₂, however, the superconductivity develops

on the far side of the phase diagram. At ambient pressure, there is no evidence of superconductivity down to the lowest measured temperature. If and to what extent the f electrons may participate in the Cooper pairing remains to be examined in the future. On the other hand, valence fluctuations may also play a role and even promote the pairing^{3,41}. In $\text{CeCu}_2(\text{Si}_{1-x}\text{Ge}_x)_2$ and CeAu_2Si_2 , superconductivity extends to very high pressure far away from the magnetic QCP with a greatly enhanced T_c ^{3,8,9}. It is thus speculated that superconductivity in CeCuP_2 near P_{c2} or P_{c3} may potentially involve a valence mechanism.

Discussion

Putting together, our systematic measurements can be summarized in the overall P - T phase diagram presented in Figs. 1(a) and 1(b), indicating a rich variation in the electronic properties of CeCuP_2 at ambient and high pressure, which is not only different from most other Ce-based HF compounds but also beyond the conventional Doniach paradigm. At ambient pressure, a crossover drives this system from NFL to FL, which is not well understood so far. Scaling analysis demonstrates the quantum critical behavior at ambient pressure and zero field. With increasing pressure, the Kondo coherence state is first suppressed, in contrast to most Ce-based HF compounds, and an intermediate Kondo semi-metallic state emerges in the intermediate pressure region, before a second metallic state emerges at even higher pressures. The unusual phase diagram may be associated with the particular crystal, low-carrier and mixed-valence properties of CeCuP_2 . The fractional occupancies of the crystal sites provide a rare platform apt for chemical tuning. On the other hand, the low carrier density usually favors a magnetically ordered state. Recent experiments on the HF material $\text{CeNi}_{1.2-\delta}\text{As}_2$ with a low carrier density of $\sim 0.032 e^-$ per formula unit observed a pressure-induced

quantum phase transition from an AFM order to a coherent Kondo screening state ²², with T_{coh} emerging and increasing with pressure across the QCP, in line with predictions of the Doniach picture. Thus, the low carrier density alone cannot explain the unusual phase diagram in CeCuP₂ and it might be essential to consider other key factors.

Since the Ce ions are in a mixed-valence state, we speculate that not only the Kondo hybridization but also the Ce valence is tuned by pressure, which would in turn affect the carrier concentration and the ground state of CeCuP₂. As a matter of fact, following previous analysis on CeCu₂Si₂ and CeRhGe₃ ^{43,44}, we find a rough resistivity scaling that tentatively points towards a potential pressure-induced valence transition near P_{c1} in CeCuP₂ (Supplementary Fig. 10). More details can be found in the Supplementary Information ¹³. If this is the case, the system can no longer be described by the usual Kondo lattice model, which ignores the charge degrees of freedom of the Ce-ions ³. This might cause the breakdown of the Doniach picture. As proposed by Hattori, pressure can drive the ground state of HFs from heavy Fermi liquid to “light” Fermi liquid, where the effective mass is smaller than that in the former, across a first-order meta-orbital transition based on both a two-orbital Anderson lattice model and the self-consistent renormalization (SCR) theory ¹¹. For CeCuP₂, the temperature dependence of the resistivity displays typical heavy-fermion behavior. Under high pressure where the superconducting transitions occur, the resistivity shows typical metallic behavior, and the f -electrons may be partially decoupled from the conduction electrons and localized. The small magnitude of the initial upper critical field slopes further indicates conventional superconducting pairing as well as a “light” effective mass compared with other HF superconductors, although this quantity can be affected by disorder and the nonzero resistance. We nonetheless get strong hints that CeCuP₂ is on the left side of the first-order transition line, and pressure drives it

from heavy Fermi liquid to “light” Fermi liquid across the transition. In the temperature dependence of the resistivity, the valence fluctuations lead to a T^n ($n = 1, 4/3, 5/3$) dependence near the critical end point (CEP). We then check the temperature dependence of the resistivity (R/R_{300K}) for CeCuP₂ at several critical pressures, as shown in Supplementary Fig. 11, finding a T^n ($n > 2$) dependence, which is beyond the SCR picture. Moreover, the P - T phase diagrams obtained here is also different from other Ce-based HF compounds with potential valence instabilities, e.g., CeCu₂(Si_{1-x}Ge_x)₂, CeAu₂Si₂, and possibly also CeIrIn₅^{3,8,9,41}. It therefore remains to be understood with more sophisticated models. The superconductivity with enhanced T_c at high pressures might only be fully explained when the valence or other effects are taken into consideration. All these special features make CeCuP₂ a unique platform for studying the rich variety of heavy fermion physics beyond the usual Doniach paradigm.

Methods

Sample preparation. High-purity starting materials of Ce powder (99.9%, Alfa Aesar), Cu powder (99.9%, Alfa Aesar), P flakes (99.999 %, Aladdin) and Sn powder (99.99%, Aladdin) were mixed in a molar ratio of 1 : 1 : 10 : 60 and loaded into an alumina crucible, which was sealed under vacuum in a quartz ampoule. The sealed ampoule was very slowly heated to 1150°C and kept there for 3 days, then cooled at a rate of 1.5 °C/h. The ampoule was taken out and the excess Sn flux decanted with a centrifuge at 500°C. LaCuP₂ is prepared by an arc-melting method. High-purity starting materials of La chunk (99.9%, Alfa Aesar), Cu lump (99.9%, Alfa Aesar), P flakes (99.999%, Aladdin) in a molar ratio of 1 : 1.15 : 5 were loaded in a water-cooled copper boat, and the mixture was then arc-melted several times. The obtained compound was ground in a glove box, and the powder was

pressed into pills. These pills were sealed in a quartz ampoule, and then annealed at 1000°C for 3 days. Chemical composition and crystal structure determinations can be found in the Supplementary Information¹³.

Electrical transport and thermodynamics measurements. Resistance measurements from 300 to 2 K and below 2 K were performed in a physical property measurement system (PPMS; Quantum Design) and a ³He cryostat, respectively. *dc* magnetic susceptibility measurements were performed in a magnetic property measurement system (MPMS; Quantum Design) equipped with a ³He cryostat, with magnetic field applied perpendicular to the *ab* plane of the CeCuP₂ single crystal. *ac* magnetic susceptibility measurements were performed in a PPMS equipped with a dilution refrigerator. Heat capacity measurements were conducted using the relaxation method in a PPMS equipped with a ³He cryostat and magnetic field was also applied along *c* axis of the CeCuP₂ single crystal.

Pressure measurements. For high-pressure experiments, samples were loaded in a piston-cylinder clamp cell made of Be-Cu alloy, with Daphne oil as the pressure medium. The pressure inside the cell was determined from the *T_c* of a tin wire. A CeCuP₂ single crystal was cut into a bar shape, and the standard four-probe method was used for resistivity measurements, with contacts made using silver epoxy. Higher-pressure measurements were performed on powder samples comprising crushed single crystals using a diamond anvil cell (DAC). For Run1 measurements, no pressure transmitting medium was adopted, while, for Run2 measurements, NaCl was used as the pressure transmitting medium. The experimental pressures were determined by the pressure-induced fluorescence shift of ruby² at room temperature before and after each experiment. A direct-current van der Pauw

technique was adopted.

Data availability

The data that support the findings of this study are available from the corresponding author upon reasonable request.

References

1. Hewson, A. C. & Coleman, P. The Kondo Problem of Heavy Fermions. *Physics Today* **47**, 60-61(1993).
2. Si, Q. M. & Steglich, F. Heavy fermions and quantum phase transitions. *Science* **329**, 1161-1166 (2010).
3. Weng, Z. F. *et al.* Multiple quantum phase transitions and superconductivity in Ce-based heavy fermions. *Rep. Prog. Phys.* **79**, 094503 (2016).
4. Phan, V.-N. Superconductivity in Ce-based heavy-fermion systems under high pressure. *Phys. Rev. B* **101**, 245120 (2020).
5. Helm, T. Non-monotonic pressure dependence of high-field nematicity and magnetism in CeRhIn₅. *Nat. Commun.* **11**, 3482 (2020).
6. Braithwaite, D. Multiple superconducting phases in a nearly ferromagnetic system. *Commun. Phys.* **2**, 147 (2019).
7. Doniach, S. The Kondo lattice and weak antiferromagnetism. *Physica B+ C* **91**, 231-234 (1977).
8. Yuan, H. Q. *et al.* Non-Fermi liquid states in the pressurized CeCu₂(Si_{1-x}Ge_x)₂ system: two critical points. *Phys. Rev. Lett.* **96**, 047008 (2006).

9. Ren, Z. *et al.* Giant overlap between the magnetic and superconducting phases of CeAu₂Si₂ under pressure. *Phys. Rev. X* **4**, 031055 (2014).
10. Pourovskii, L. V., Hansmann, P., Ferrero, M. & Georges, A. Theoretical prediction and spectroscopic fingerprints of an orbital transition in CeCu₂Si₂. *Phys. Rev. Lett.* **112**, 106407 (2014).
11. Hattori, K. Meta-orbital transition in heavy-fermion systems: analysis by dynamical mean field theory and self-consistent renormalization theory of orbital fluctuations. *J. Phys. Soc. Jpn.* **79**, 114717 (2010).
12. Chykhrij, S. I., Loukashouk, G. V., Oryshchyn, S. V., Kuz'ma, Y. B. Phase equilibria and crystal structure of compounds in the Ce-Cu-P system. *J. Alloy. Compd.* **248**, 224-232 (1997).
13. Supplementary Information to 'Quantum phase transitions and superconductivity in the pressurized heavy-fermion compound CeCuP₂'.
14. Desgranges, H. & Schotte, K. Specific heat of the Kondo model. *Phys. Lett. A* **91**, 240-242 (1982).
15. Sengupta, K. *et al.* Magnetic, electrical resistivity, heat-capacity, and thermopower anomalies in CeCuAs₂. *Phys. Rev. B* **70**, 064406 (2004).
16. Cvitkovich, L. *et al.* Anisotropic Physical Properties of the Kondo Semimetal CeCu_{1.11}As₂. *J. Phys. Soc. Jpn.* **30**. 011020 (2020).
17. Gegenwart, P. *et al.* Ferromagnetic quantum critical fluctuations in YbRh₂(Si_{0.95}Ge_{0.05})₂. *Phys. Rev. Lett.* **94**, 076402 (2005).

18. Ernsting, D. *et al.* Vacancies, disorder-induced smearing of the electronic structure, and its implications for the superconductivity of anti-perovskite $\text{MgC}_{0.93}\text{Ni}_{2.85}$. *Sci. Rep.* **7**, 10148 (2017).
19. Kuo, C. N. *et al.* Lattice distortion associated with Fermi-surface reconstruction in $\text{Sr}_3\text{Rh}_4\text{Sn}$. *Phys. Rev. B* **91**, 165141 (2015).
20. Nozières, P. Magnetic impurities and the Kondo effect. *Ann. Phys. Fr.* **10**, 19-35 (1985).
21. Nozières, P. Some comments on Kondo lattices and the Mott transition. *Eur. Phys. J. B* **6**, 447-457 (1998).
22. Luo, Y. K. *et al.* Pressure-tuned quantum criticality in the antiferromagnetic Kondo semimetal $\text{CeNi}_{2-\delta}\text{As}_2$. *P. Natl. Acad. Sci. USA* **112**, 13520-13524 (2015).
23. Zhang, P. *et al.* Protracted Kondo coherence with dilute carrier density in Cerium based nickel pnictides. Preprint at: <http://arxiv.org/abs/1909.13251> (2019).
24. Shaginyan, V. R., Amusia, M. Y., Msezane, A. Z., Popov, K. G. Scaling behaviour of heavy fermion metals. *Phys. Rep.* **492**, 31-109 (2010).
25. Matsumoto, Y. *et al.* Quantum criticality without tuning in the mixed valence compound $\beta\text{-YbAlB}_4$. *Science* **331**, 316-319 (2011).
26. Wu, L. S. *et al.* Quantum critical fluctuations in layered $\text{YFe}_2\text{Al}_{10}$. *P. Natl. Acad. Sci. USA* **111**, 14088-14093 (2014).
27. Koerner, S. *et al.* Crossover to Fermi-liquid behavior at lowest temperatures in pure CeNi_2Ge_2 . *J. Low Temp. Phys.* **119**, 147-153 (2000).
28. Gegenwart, P. Grüneisen parameter studies on heavy fermion quantum criticality. *Rep. Prog. Phys.* **79**, 114502 (2016).

29. Yang, Y.-F. *et al.* Scaling the Kondo lattice. *Nature* **454**, 611-613 (2008).
30. Yang, Y.-F., Pines, D. & Lonzarich, G. Quantum critical scaling and fluctuations in Kondo lattice materials. *P. Natl. Acad. Sci. USA* **114**, 6250-6255 (2017).
31. Hegger, H. *et al.* Pressure-induced superconductivity in quasi-2D CeRhIn₅. *Phys. Rev. Lett.* **84(21)**, 4986 (2000).
32. Thomas, S. M. *et al.* Evidence for a pressure-induced antiferromagnetic quantum critical point in intermediate valence UTe₂. *Sci. Adv.* **6**, eabc8709 (2020).
33. Mani, A. *et al.* Pressure-induced superconductivity in BaFe₂As₂ single crystal. *EPL* **87**, 17004 (2009).
34. Gofryk, K. *et al.* Local inhomogeneity and filamentary superconductivity in Pr-doped CaFe₂As₂. *Phys. Rev. Lett.* **112**, 047005 (2014).
35. Petrovic, C. *et al.* Heavy-fermion superconductivity in CeCoIn₅ at 2.3 K. *J. Phys.: Condens. Matter* **13**, L337-L342 (2001).
36. Clogston, A. M. Upper limit for the critical field in hard superconductors. *Phys. Rev. Lett.* **9**, 266-267 (1962).
37. Chandrasekhar, B. S. A note on the maximum critical field of high-field superconductors. *Appl. Phys. Lett.* **1**, 7-8 (1962).
38. Pressure-induced superconductivity in an antiferromagnet CeRh₂Si₂. *J. Phys.: Condens. Matter* **14**, L377-L383 (2002).
39. Sheikin, I. *et al.* Superconductivity, upper critical field and anomalous normal state in CePd₂Si₂ near the quantum critical point. *J. Low Temp. Phys.* **122**, 591-604 (2001).

40. Das, D. *et al.* Magnetic field driven complex phase diagram of antiferromagnetic heavy-fermion superconductor Ce₃PtIn₁₁. *Sci. Rep.* **8**, 16703 (2018).
41. Watanabe, S. & Miyake, K. Roles of critical valence fluctuations in Ce- and Yb-based heavy fermion metals. *J. Phys.: Condens. Matter* **23**, 094217 (2001).
42. Yuan, H. Q. *et al.* Observation of two distinct superconducting phases in CeCu₂Si₂. *Science* **302**, 2104-2107 (2003).
43. Seyfarth, G. *et al.* Heavy fermion superconductor CeCu₂Si₂ under high pressure: Multiprobing the valence crossover. *Phys. Rev. B* **85**, 205105 (2012).
44. Wang, H. H. *et al.* Anomalous connection between antiferromagnetic and superconducting phases in the pressurized noncentrosymmetric heavy-fermion compound CeRhGe₃. *Phys. Rev. B* **99**, 024504 (2019).

Acknowledgements

We thank G. M. Zhang and C. Petrovic for their helpful discussions. This work is supported by the Ministry of Science and Technology of China (Grants No. 2016YFA0300503, No. 2017YFA0303103), the NSAF (Grant No. U1630248), the National Natural Science Foundation of China (Grant No. 11674367, No. 11774401), the Shanghai Municipal Science and Technology Major Project (Grant No. 2019SHZDZX01), and the Zhejiang Provincial Natural Science Foundation (Grant No. LZ18A040002). DCP is supported by the Chinese Academy of Sciences through 2018PM0036.

Author Contributions

S.Y.L. and E.J.C. conceived the idea and designed the experiments. E.J.C. was responsible for single-crystal growth and ambient/high-pressure transport experiments. C.C.Z., T.P.Y., J.M.N., B.L.P., Y.Y.H. and L.S.W. participated in the collection of data. T.P.Y. conducted the Rietveld refinement of powder X-ray diffraction. E.J.C., S.Y.L., Y.F.Y., Y.J.X., T.P.Y. and D.C.P. analyzed the data. E.J.C., D.C.P., S.Y.L. and Y.F.Y. wrote the manuscript. All authors discussed the results and commented on the manuscript.

Competing interests

The authors declare no competing interests.

Additional Information

Supplementary information is available for this paper at URL inserted when published.

Correspondence and requests for materials should be addressed to Y.-F.Y. (yifeng@iphy.ac.cn) or S.Y. L. (shiyang_li@fudan.edu.cn).

Figure 1

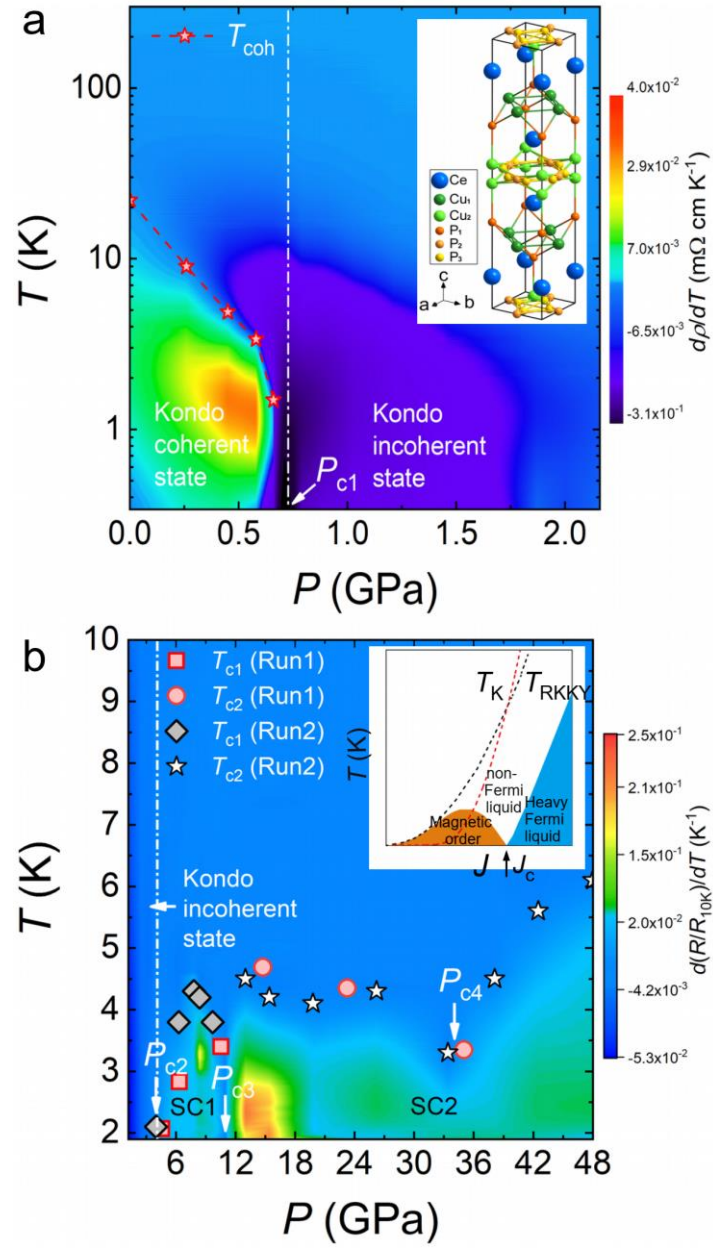


Figure 2

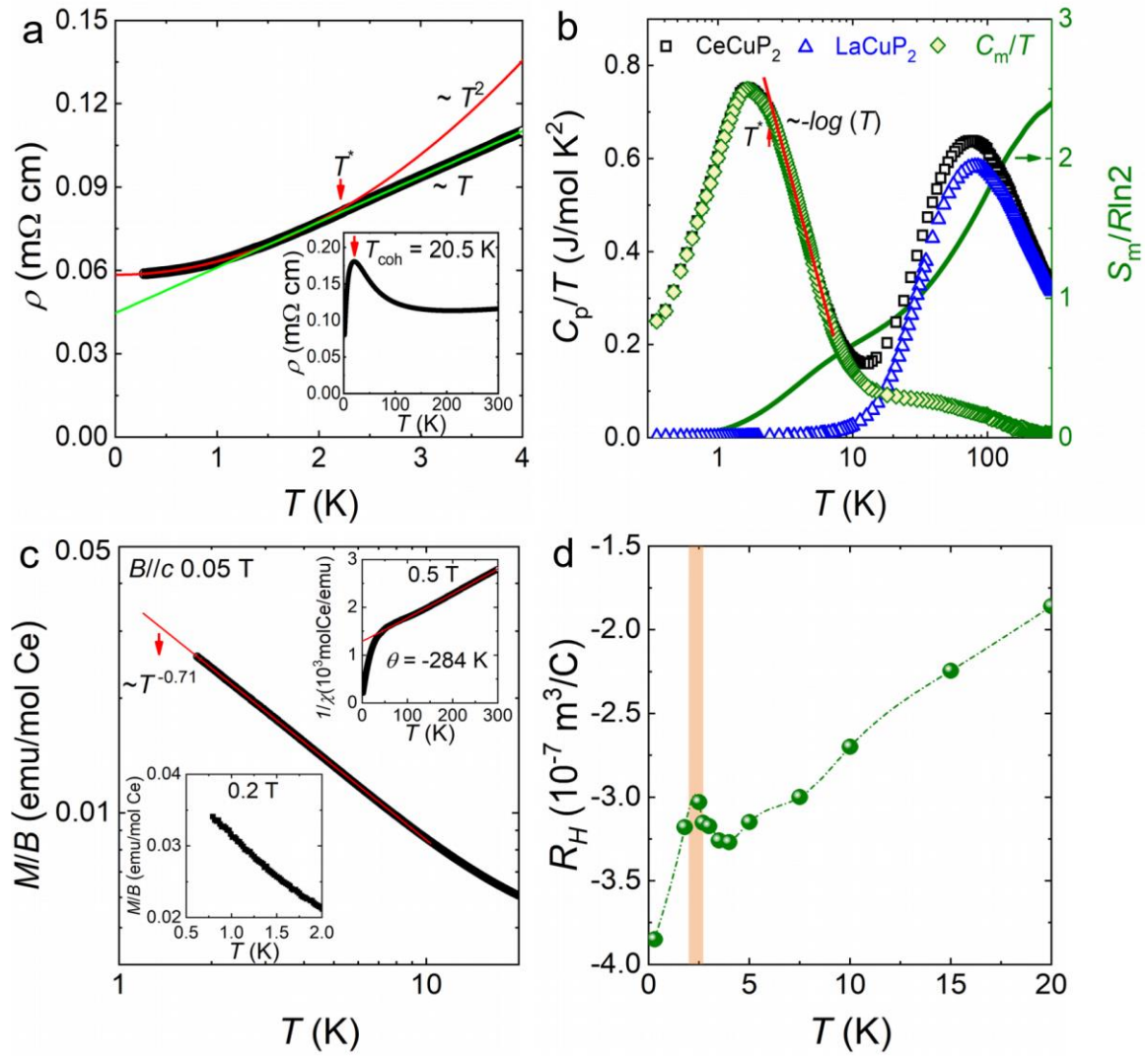


Figure 3

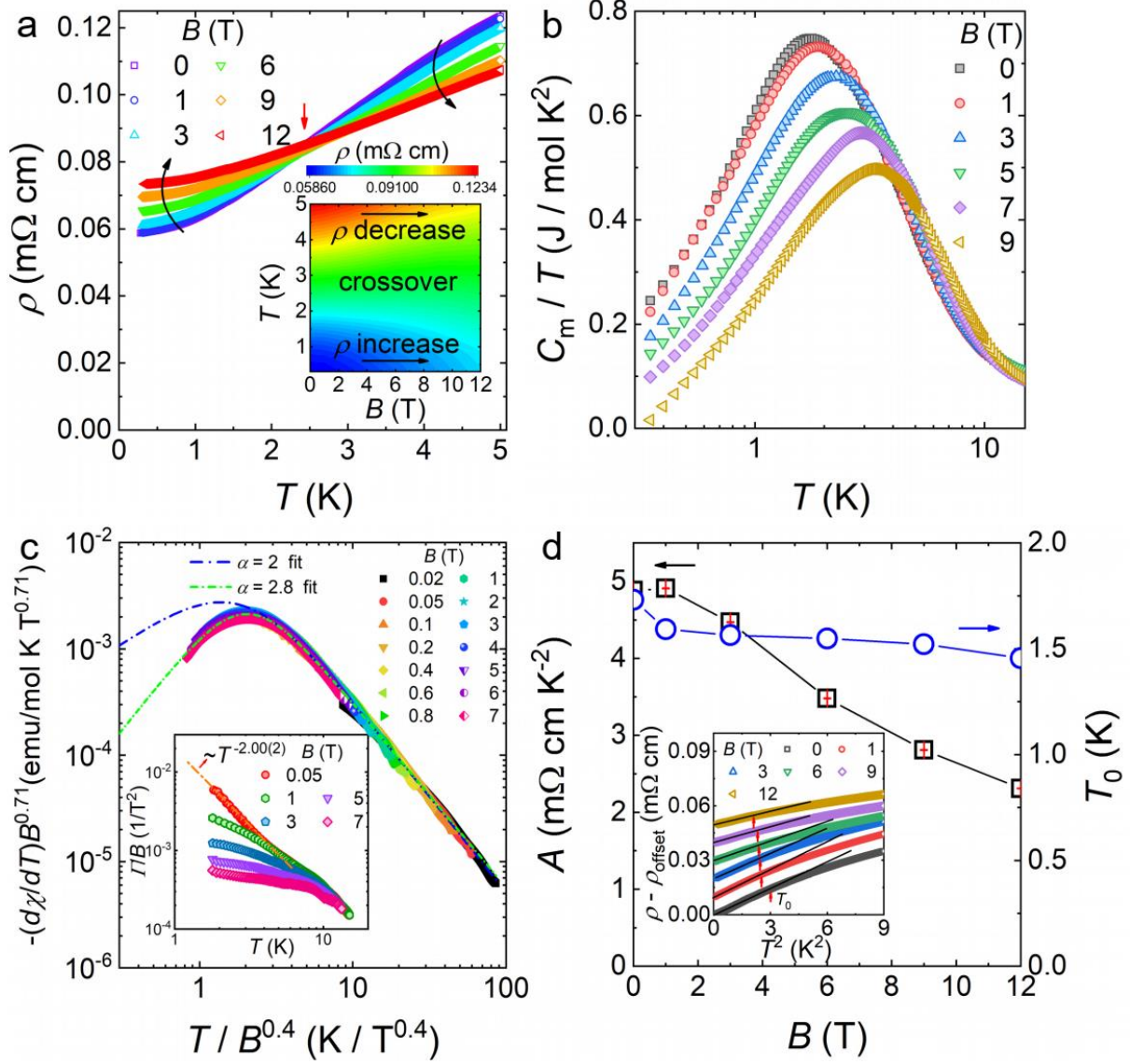


Figure 4

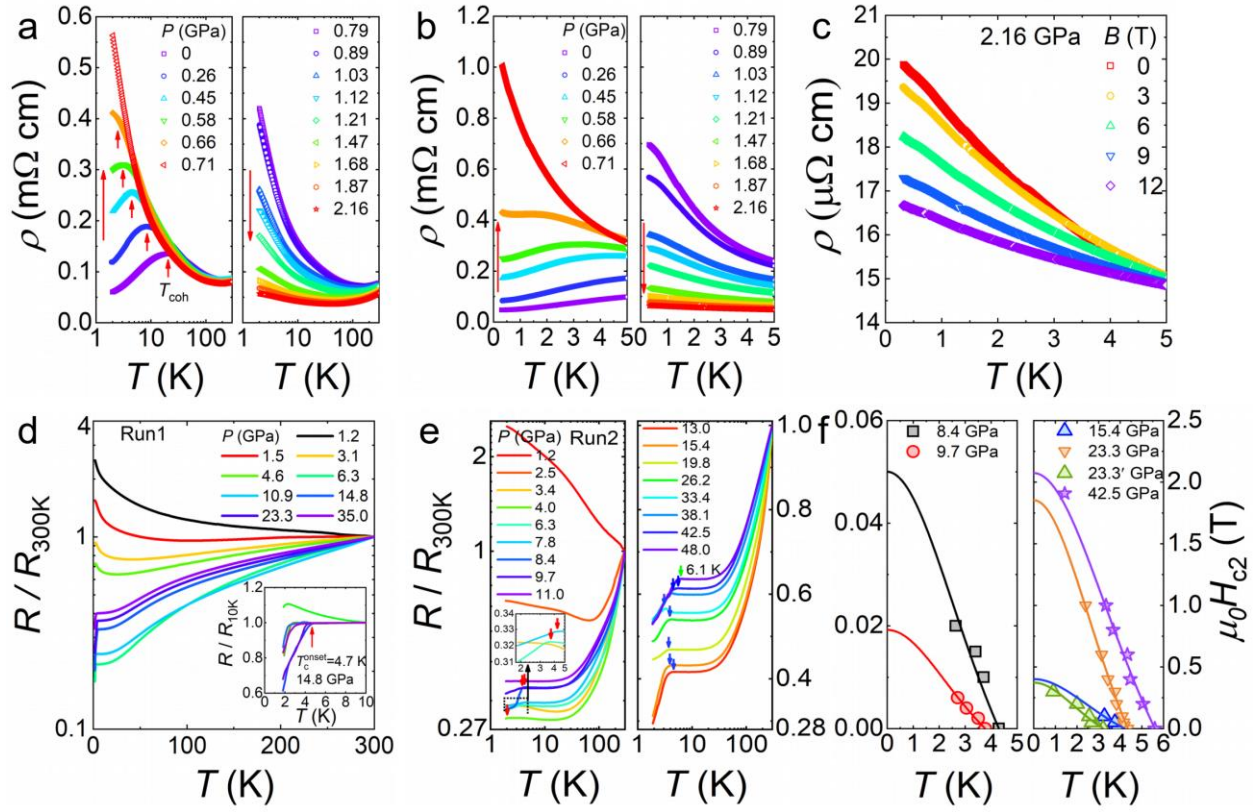


Figure captions

Figure 1. Pressure-temperature (P - T) phase diagrams of CeCuP₂. **a** P - T phase diagram of the CeCuP₂ single crystal under low pressure. The pressure dependence of coherence temperature (T_{coh}) taken from Fig. 4(a) is added, and the color represents the magnitude of $d\rho/dT$. For pressures $P < P_{c1}$, the system remains in a Kondo coherent state. For $P > P_{c1}$, a Kondo incoherent state takes over. Inset shows the crystal structure of CeCuP₂. CeCuP₂ crystallizes in a tetragonal structure (space group: $I4/mmm$ (No. 139)) with three different P sites, two differing Cu sites but only one Ce atomic position. **b** P - T phase diagram of CeCuP₂ powder obtained by crushing single crystals, under higher pressure. Run1 and Run2 denote resistance measurements without pressure transmitting medium and with NaCl as the pressure transmitting medium, respectively. For $1.2 \text{ GPa} < P < P_{c2}$, the system remains in a Kondo incoherent state. At P_{c2} , superconductivity appears. For $P_{c2} \leq P < P_{c3}$, the system is in the first superconducting state (SC1). At $P_{c3} \sim 11.0 \text{ GPa}$, the first SC1 disappears. With increasing pressure beyond P_{c3} , the second superconducting state (SC2) arises. Upon further compression to a critical pressure (P_{c4}) of $\sim 34.0 \text{ GPa}$, the T_c^{onset} defined according to the onset of the transition for SC2 reaches a minimum, and then it goes up to 6.1 K at 48.0 GPa . The background color represents the magnitude of $d(R/R_{10\text{K}})/dT$ taken from Run2 measurements. Inset shows the regular Doniach phase diagram ⁷.

Figure 2. Physical properties of CeCuP₂ single crystal under ambient pressure. **a** In-plane resistivity of a CeCuP₂ single crystal from 0.3 to 4 K in zero field. The green and red lines represent linear and quadratic fits, respectively, and indicates that the ground state of CeCuP₂ is a Fermi liquid. A characteristic temperature (T^*) denotes the crossover from non-Fermi liquid to Fermi liquid

behavior. Inset shows the resistivity up to 300 K, which displays typical Kondo heavy-fermion behavior with a coherence temperature of 20.5 K. **b** Specific heats of CeCuP₂, LaCuP₂ and magnetic specific heat (C_m/T) extracted by deducting the electron and phonon contributions in LaCuP₂ from those in CeCuP₂. The red line represents the $-\log(T)$ dependence. The green line denotes the magnetic entropy (S_m) calculated based on C_m/T . The red arrow marks the characteristic temperature (T^*) where it deviates from $-\log(T)$, corresponding to that in the resistivity. **c** Temperature dependence of the *dc* susceptibility measured at 0.05 T. The solid line shows the low-field fitting with a $T^{-0.71}$ divergence. Right inset shows the reciprocal susceptibility from 1.8 to 300 K measured at 0.5 T, and the red solid line represents the Curie-Weiss fit, which yields a Weiss temperature (θ) of -284 K, indicating antiferromagnetic interactions. Left inset shows the low-temperature data at 0.2 T below 2 K, excluding long-range magnetic order. **d** Hall coefficient (R_H) obtained by fitting the data of Hall resistivity from 0 to 3 T. The negative R_H indicates that electron carriers dominate. On cooling from 20 to 4 K, the magnitude of R_H increases monotonously. Subsequently, a peak situating ~ 2.4 K emerges abruptly. The shadowed area marks the change in the R_H . The carrier concentration at 0.3 K can be estimated to be $1.97 \times 10^{19} \text{ cm}^{-3}$.

Figure 3. Physical properties of CeCuP₂ single crystal under magnetic field. **a** In-plane resistivity of CeCuP₂ under magnetic fields applied along the *c* axis. Under magnetic fields, the resistivity curves meet in a point at ~ 2.4 K, below which the magnetoresistance (MR) is positive, and above which it is negative. Inset shows a contour plot of the temperature dependence of the resistivity at several magnetic fields; the green area represents the crossover where the MR changes sign. **b** Magnetic specific heat of CeCuP₂ single crystal under magnetic field applied along the *c* axis.

c Scaling collapse of the temperature derivative of χ multiplied by $B^{0.71}$ as a function of the variable $T/B^{0.4}$. Inset shows the Grüneisen ratio Γ divided by B . **d** Field dependence of the T^2 coefficient A (in $\Delta\rho = AT^2$), and the upper limit of the T^2 range, T_0 (arrows in the inset). Inset displays the temperature dependence of the resistivity at low temperature, plotted as $\rho(T) - \rho_{\text{offset}}$ vs. T^2 , at several magnetic fields. ρ_{offset} is a constant arbitrary offset chosen for clarity of display. The solid lines are linear fits to the data below T_0 . The slope of these lines is the inelastic electron-electron scattering coefficient A .

Figure 4. Electrical transport measurements of CeCuP₂ under pressure, and emergence of superconductivity. Resistivity of a CeCuP₂ single crystal at different pressures, **(a)** from 2 to 300 K and **(b)** from 0.3 to 5 K. Upon increasing the pressure from 0 to 0.71 GPa, the Kondo coherence temperature monotonically decreases. Above 0.71 GPa, the resistivity decreases with increasing pressure. **c** Temperature dependence of the resistivity under 2.16 GPa at several magnetic fields. With increasing field, the resistivity monotonically decreases, in contrast to the behavior at ambient pressure, as plotted in Fig. 3(a). **d** Temperature dependence of the normalized resistance of CeCuP₂ powder obtained by crushing single crystals obtained by crushing a single crystal at higher pressures without pressure transmitting medium (denoted as Run1). Inset shows the superconducting transitions, and the arrow marks the onset transition temperature T_c^{onset} of 4.7 K at 14.8 GPa. **e** Resistance measurements of CeCuP₂ powder obtained by crushing single crystals at higher pressures with NaCl as the pressure transmitting medium (denoted as Run2). **f** Temperature dependence of the upper critical field $\mu_0 H_{c2}$ at several pressures. 23.3 GPa in right panel denotes the data that superconducting transition temperature is defined according to a 10% drop ($T_c^{10\%}$). Lines represent the Ginzburg-Landau fit.

Supplementary Information to
“Quantum phase transitions and superconductivity in the
pressurized heavy-fermion compound CeCuP₂”

Erjian Cheng¹, Chuchu Zhu¹, Tianping Ying¹, Yuanji Xu², Darren C. Peets³, Jiamin Ni¹, Binglin

Pan¹, Yeyu Huang¹, Linshu Wang¹, Yi-feng Yang^{2,*} and Shiyun Li^{1,4,5,*}

¹ *State Key Laboratory of Surface Physics, Department of Physics, Fudan University, Shanghai 200438, China*

² *Beijing National Laboratory for Condensed Matter Physics and Institute of Physics, Chinese Academy of Sciences, Beijing 100190, China*

³ *Ningbo Institute of Materials Technology and Engineering, Chinese Academy of Sciences, Ningbo, Zhejiang 315201, China*

⁴ *Collaborative Innovation Center of Advanced Microstructures, Nanjing 210093, China*

⁵ *Shanghai Research Center for Quantum Sciences, Shanghai 201315, China*

Supplementary Note 1: Chemical composition and crystal structure determinations

The chemical composition of the CeCuP₂ single crystals is Ce : Cu : P = 1 : 1.14 : 2 as determined by inductively coupled plasma (ICP) spectroscopy. We performed Rietveld refinement of powder X-ray diffraction (XRD) data obtained by crushing several single crystals of CeCuP₂, as shown in Supplementary Fig. 1(a). Fractional occupancies are expected for the Cu₂, P₂, and P₃ atoms¹. For Rietveld refinement,

we use the results of ICP, i.e., Ce : Cu = 1 : 1.14, as fixed parameters, while the P stoichiometry is taken as a free parameter because of its higher uncertainty as a light element. The Rietveld refinement of CeCuP₂ gives the refined crystallographic parameters shown in Supplementary Table 1, with $R_p = 4.17$, $R_{wp} = 6.46$, $R_{exp} = 4.01$ and $\chi^2 = 2.6$. Based on the refinement, the P stoichiometry is 2.186(6), yielding Ce : Cu : P = 1 : 1.14 : 2.186(6), which is slightly higher than ICP. The crystal structure shown in the main text (inset to Fig. 1(a)) is based on this refinement. The crystal structure of LaCuP₂ has also been checked by XRD, and the chemical composition of LaCuP₂ was determined to be 1 : 1.11 : 1.9 by EPMA.

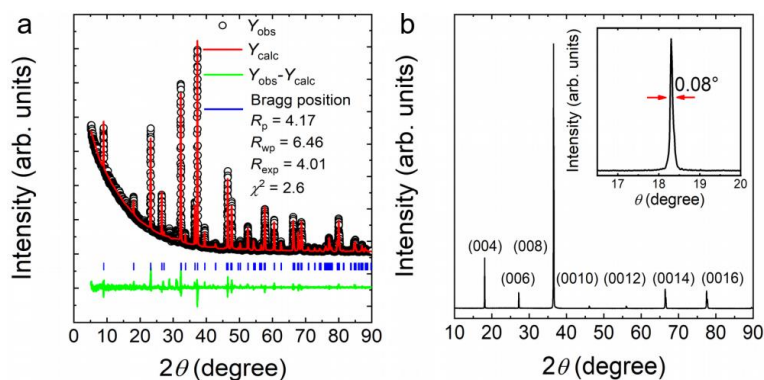
The largest surface of a CeCuP₂ single crystal is indexed to the (00 l) plane, as plotted in Supplementary Fig. 1(b). The inset to Supplementary Fig. 1(b) shows the X-ray rocking curve of the (008) peak with the full width at half maximum (FWHM) of 0.08 °, indicative of the high quality of our samples.

Compound		CeCuP ₂ (space group: $I4/mmm$ (139))	
Atoms	(x/a, y/b, z/c)	occupancy ratio	Wyckoff Positions
Ce	(0, 0, 0.11845(5))	1.000(0)	4e
Cu1	(0.5, 0, 0.25)	1.000(0)	4d
Cu2	(0, 0, 0.46424(8))	0.140(0)	4e
P1	(0, 0, 0.32038(3))	1.000(0)	4e
P2	(0.5, 0, 0)	0.654(2)	4c
P3	(0.31867(1), 0, 0.5)	0.266(2)	8j
Cell parameters		Refinement parameters	
a (Å)	3.90663(6)	R_p	4.17

b (Å)	3.90663(6)	R_{wp}	6.46
c (Å)	19.6578(4)	R_{exp}	4.01
V (Å ³)	300.012(8)	χ^2	2.6

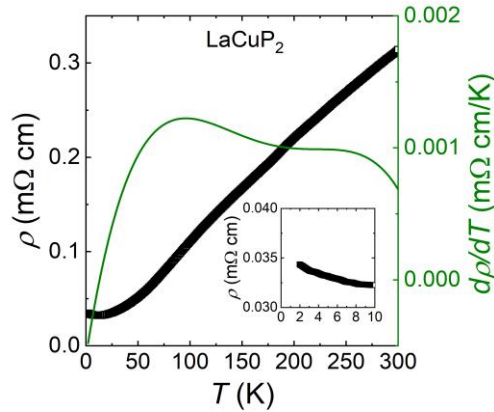
Supplementary Table 1. Crystallographic parameters of CeCuP₂.

Supplementary Note 2: XRD measurements



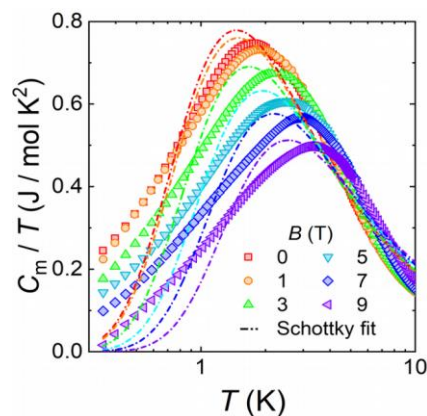
Supplementary Figure 1. XRD measurements of CeCuP₂. **a** Rietveld refinement of powder XRD of CeCuP₂ obtained by crushing several single crystals. The Rietveld refinement successfully converges to $R_p = 4.17$, $R_{wp} = 6.46$, $R_{exp} = 4.01$ and 2.6. **b** XRD pattern from the largest surface of a CeCuP₂ single crystal. Only (00 l) Bragg peaks are observed. Inset shows the X-ray rocking curve of the (008) peak.

Supplementary Note 3: Resistivity of LaCuP₂



Supplementary Figure 2. Resistivity of polycrystalline LaCuP₂ at ambient pressure. The resistivity shows a metallic behavior from 10 to 300 K, and then displays semi-metallic behavior below 10 K. The derivative result of resistivity has also been displayed, and one can see an anomaly around 100 K, which may be related to the charge-density-wave (CDW) transition, but more evidence would be required. To check this, Hall resistivity and detailed theoretical analysis are called for.

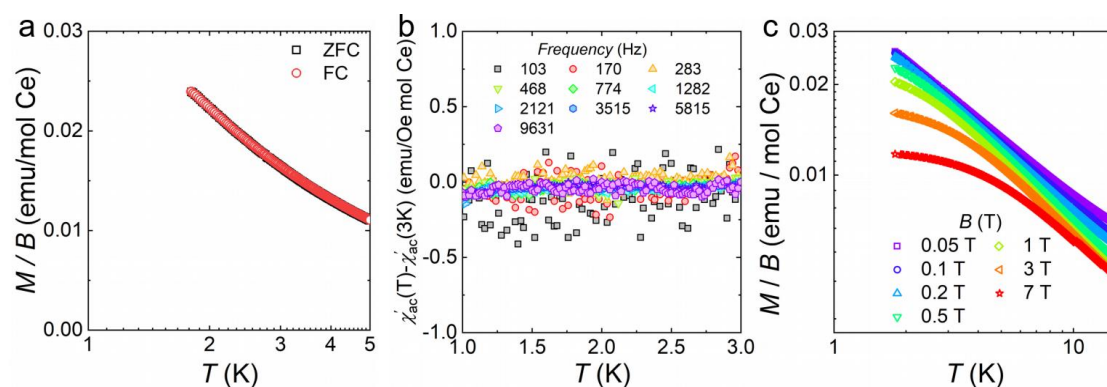
Supplementary Note 4: Specific heat measurements under magnetic field



Supplementary Figure 3. The C_m/T of a CeCuP₂ single crystal at various magnetic fields. The broken lines represent the fits according to a two-level Schottky function³. Obviously, the hump in CeCuP₂ contradicts the prediction of the Schottky

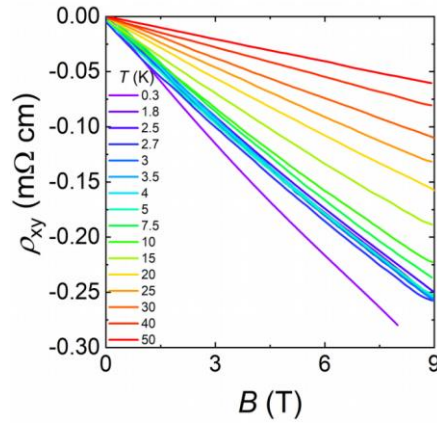
function for all fixed magnetic fields.

Supplementary Note 5: *dc* and *ac* magnetic susceptibility measurements



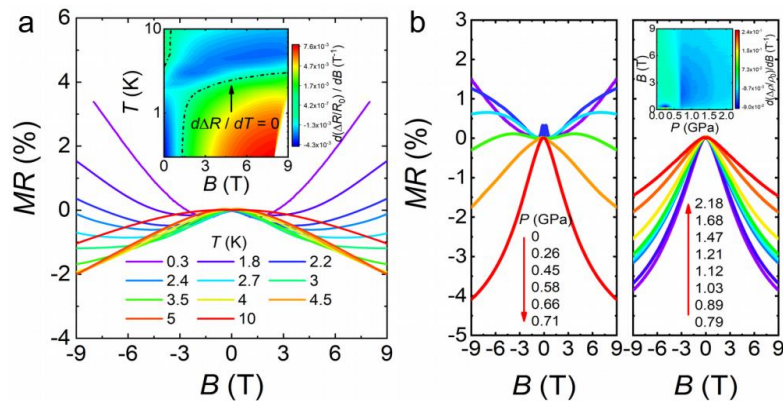
Supplementary Figure 4. *dc* and *ac* magnetic susceptibility of CeCuP₂ single crystal. **a** Zero field cooling (ZFC) and field cooling (FC) of *dc* magnetic susceptibility of CeCuP₂ single crystal from 1.8 K to 5 K with magnetic field applied along *c* axis. **b** *ac* magnetic susceptibility of CeCuP₂ single crystal. From *dc* and *ac* magnetic susceptibility, long- and short-range magnetic transitions around 1.8 K can be excluded. **c** Temperature dependence of the *dc* susceptibility under several magnetic fields.

Supplementary Note 6: Hall measurements



Supplementary Figure 5. Hall measurements of a CeCuP₂ single crystal at several fixed temperatures.

Supplementary Note 7: Magnetoresistance under ambient and high pressure



Supplementary Figure 6. Magnetoresistance (MR) of a CeCuP₂ single crystal as a function of temperature. **a** Under ambient pressure and **b** high pressures with magnetic field applied along *c* axis.

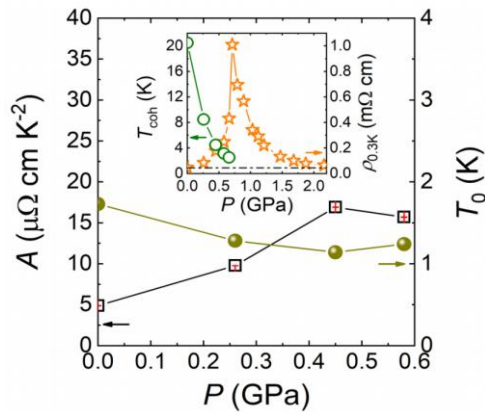
To clarify the behavior of magnetic Ce 4f electrons, the pressure dependence of

the magnetoresistance (MR) has been investigated at 2 K, as displayed in Supplementary Fig. 6(b). With increasing pressure, the MR changes from positive to negative gradually, and the curvature of the MR systematically changes. At 0.71 GPa and 9 T, the magnitude of the MR reaches a maximum. The changes in the MR from 0 to 0.71 GPa are associated with the evolution of T_{coh} . At higher pressures, the MR remains negative, but its magnitude decreases. The inset in the right panel of Supplementary Fig. 6(b) shows a contour plot of the P - B phase diagram, and there is a clear boundary at ~ 0.7 GPa, indicative of the change of the scattering mechanism under pressure, possibly associated with magnetic fluctuations. It is also worth noting that the MR in low magnetic field shows a pronounced cusp at 0.26 GPa, suggestive of a possible weak anti-localization (WAL) effect, but to verify this, Hall resistivity and detailed theoretical analysis are called for.

We attribute the change of MR from positive to negative under ambient pressure to a nonmagnetic crossover rather than magnetic fluctuations. Because, in heavy-fermion materials, the competition between a decreasing T -dependent term and an increasing T -independent residual resistivity contribution will yield a maximum in the MR of a Kondo lattice^{4,5}. At ambient pressure, the MR for CeCuP₂ shows a monotonic field dependence, rather than a maximum for all fixed temperatures (see Supplementary Fig. 6(a)), whereas, under pressure, the maximum in MR can be found at several lower pressures, characteristic of the heavy-fermion behavior, i.e., the Ce 4f electrons. Additionally, the temperature-dependent MR at 2.16 GPa (Fig. 4(c)) is in striking contrast to that at ambient pressure (Fig. 3(a)), also implying the different

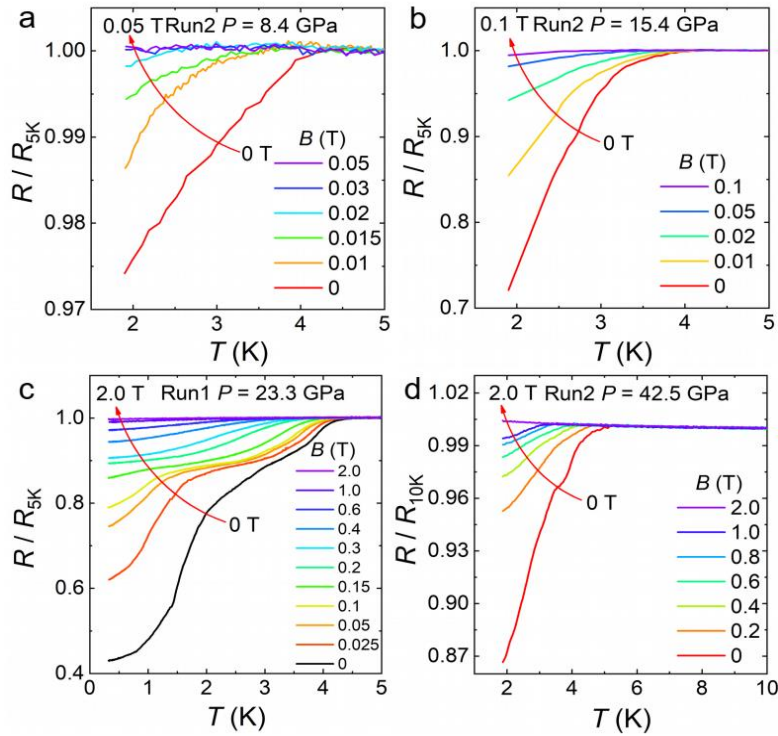
origin of scattering mechanism.

Supplementary Note 8: Pressure dependence of the electron-electron scattering coefficient A



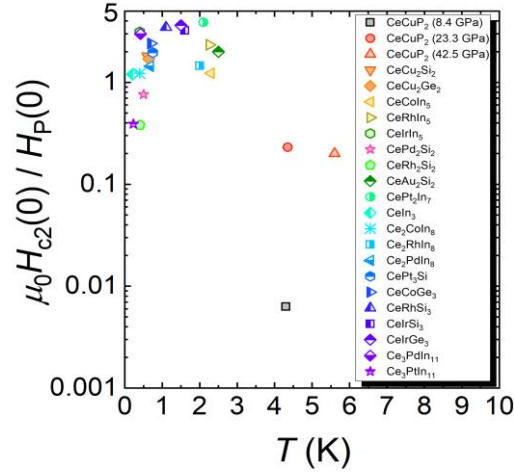
Supplementary Figure 7. Pressure dependence of the T^2 coefficient A , and the upper limit of the T^2 range, T_0 . Inset shows the pressure dependence of the T_{coh} and the resistivity at 0.3 K.

Supplementary Note 9: Magnetic field dependence of the superconducting transition at several selected pressures



Supplementary Figure 8. Magnetic field dependence of the superconducting transition at several selected pressures for CeCuP₂ powder obtained by crushing single crystals—a** 8.4 GPa; **b** 15.4 GPa; **c** 23.3 GPa; **d** 42.5 GPa. Increasing the magnetic field gradually suppresses the superconducting transition.**

Supplementary Note 10: Comparison of the upper critical field and the Pauli field for Ce-based heavy-fermion superconductors

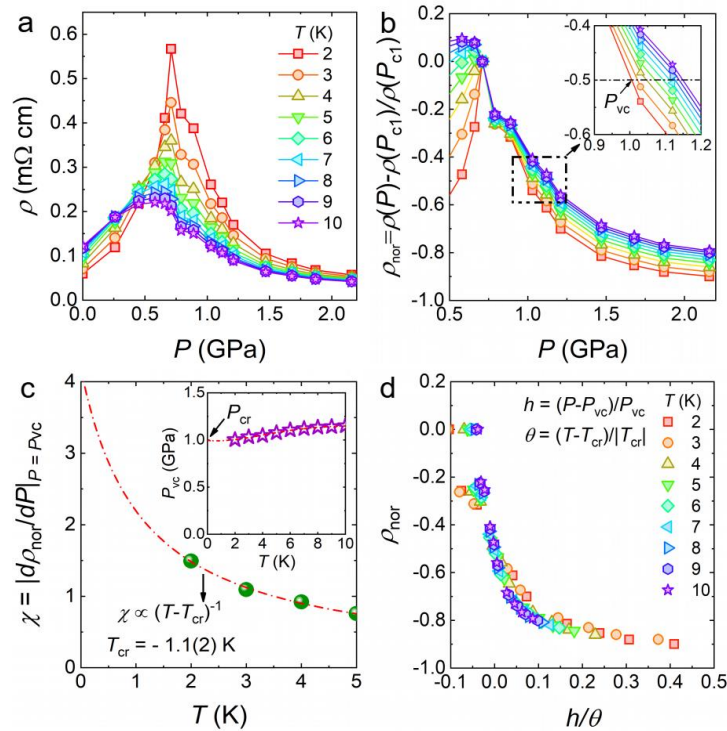


Supplementary Figure 9. Comparison of the upper critical field ($\mu_0 H_{c2}(0)$) and the Pauli field ($H_p(0)$) for Ce-based heavy-fermion superconductors. Data is taken from Refs. 6, 7 and 8 for other Ce-based heavy-fermion superconductors.

Supplementary Note 11: Scaling analysis of low-temperature resistivity at pressures near P_{c1}

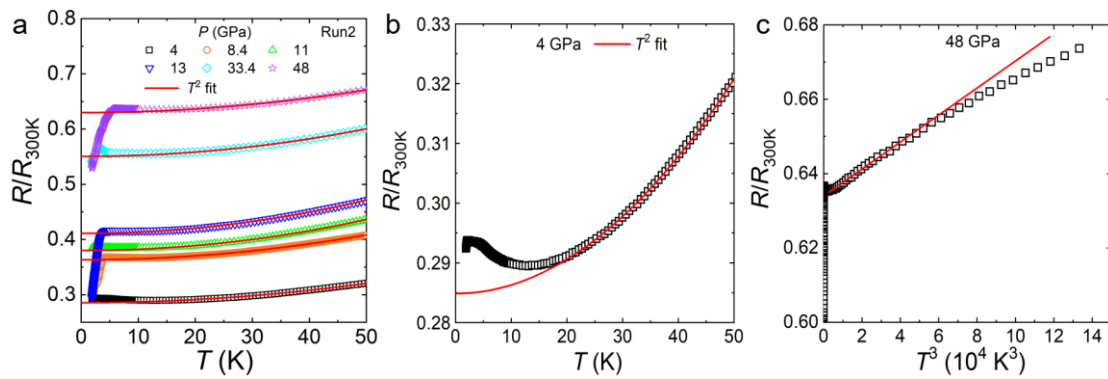
To argue the pressure-induced valence change in CeCuP₂, a scaling analysis of resistivity has been conducted according to the scaling method proposed in CeCu₂Si₂⁹ and developed in CeRhGe₃¹⁰. Different from CeCu₂Si₂ and CeRhGe₃, the resistivity above P_{c1} in CeCuP₂ is divergent on cooling, which is difficult to extract the impurity scattering contribution (i.e., residual resistivity ρ_0). Compared with the scattering of spin singlets in the incoherent state in CeCuP₂, the impurity scattering contribution can be ignored. Supplementary Fig. 9(a) plots the pressure-dependent resistivity at selected temperatures. Consistent with CeCu₂Si₂⁹ and CeRhGe₃¹⁰, the ρ begins to drop significantly above P_{c1} , implying an increased delocalization of the 4*f* electrons

in CeCuP₂. To better show the delocalization effect, a normalized resistivity ρ_{nor} ($\rho_{\text{nor}} = [\rho(P) - \rho(P_{c1})]/\rho(P_{c1})$) is defined, and the pressure-dependent ρ_{nor} is plotted in Supplementary Fig. 10(b). A pressure P_{vc} is also defined, at which ρ_{nor} drops by 50 % from its value at P_{c1} , as shown in the inset of Fig. S10(b). By extrapolating the P_{vc} data to zero temperature (inset to Supplementary Fig. 10(c)), a critical pressure $P_{\text{cr}} \sim 1$ GPa can be obtained. Supplementary Figure 10(c) shows the slope χ at P_{vc} . We fit the low-temperature points through the form $\chi \propto (T - T_{\text{cr}})^{-1}$, and obtain a critical temperature T_{cr} of -1.1(2) K. We also introduce a generalized distance h/θ , where $h = (P - P_{\text{vc}})/P_{\text{vc}}$, and $\theta = (T - T_{\text{cr}})/|T_{\text{cr}}|$, and the ρ_{nor} as a function of h/θ is plotted in Fig. S10(d). As in CeCu₂Si₂⁹ and CeRhGe₃¹⁰, the data below 10 K in CeCuP₂ shows a h/θ collapse, evidencing that the pressurized CeCuP₂ at P_{c1} is in proximity to a critical valence instability.



Supplementary Figure 10. Scaling analysis of low-temperature resistivity of a CeCuP₂ single crystal at pressures near $P_{c1} \sim 0.7$ GPa. **a** Pressure-dependent resistivity at selected temperatures. **b** Normalized resistivity ρ_{nor} as a function of pressure, where $\rho_{\text{nor}} = [\rho(P) - \rho(P_{c1})]/\rho(P_{c1})$. Inset shows the definition of the pressure P_{vc} , at which ρ_{nor} drops by 50 % from its value at P_{c1} . **c** Temperature-dependent the slope χ at P_{vc} in $\rho_{\text{nor}}-P$ curves. The red dashed line denotes a fit of $\chi \propto (T-T_{\text{cr}})^{-1}$, yielding a critical temperature T_{cr} of -1.1(2) K. Inset displays the temperature-dependent P_{vc} . By extrapolating to zero temperature, a critical pressure P_{cr} of ~ 1 GPa can be obtained. **d** Collapse of ρ_{nor} as a function of generalized distance h/θ , where $h = (P-P_{\text{vc}})/P_{\text{vc}}$, and $\theta = (T - T_{\text{cr}})/|T_{\text{cr}}|$.

Supplementary Note 12: The temperature dependence of the resistivity at several pressures



Supplementary Figure 11. Fit to the temperature dependence of the resistivity ($R/R_{300\text{K}} = \rho/\rho_{300\text{K}}$) at several pressures in Run2 measurements. Data are taken from Fig. 4(e). **a** The low-temperature resistivity ranging from ~ 15 K to 50 K

displays nearly T^2 dependence. **b** The resistivity at 4 GPa shows a low-temperature upturn, where superconductivity arises from. **c** The lower-temperature resistivity at 48 GPa displays T^3 dependence. The temperature dependence of the resistivity is beyond the self-consistent renormalization (SCR) picture.

Supplementary References

1. Chykhrij, S. I., Loukashouk, G. V., Oryshchyn, S. V., Kuz'ma, Y. B. Phase equilibria and crystal structure of compounds in the Ce-Cu-P system, *J. Alloy. Compd.* **248**, 224-232 (1997).
2. Mao, H. -K., Xu, J. A. & Bell, P. Calibration of the ruby pressure gauge to 800-kbar under quasi-hydrostatic conditions. *J. Geophys. Res.* **91**, 4673-4676 (1986).
3. Moler, K. A. Specific heat of $\text{YBa}_2\text{Cu}_3\text{O}_{7-\delta}$. *Phys. Rev. B* **55**, 6 (1996).
4. Ohkawa, F. J. Magnetoresistance of Kondo lattices. *Phys. Rev. Lett.* **64**, 2300 (1989).
5. Hu, T. *et al.* Non-Fermi liquid regimes with and without quantum criticality in $\text{Ce}_{1-x}\text{Yb}_x\text{CoIn}_5$. *P. Natl. Acad. Sci. USA* **110**, 7160 (2013).
6. Weng, Z. F. *et al.* Multiple quantum phase transitions and superconductivity in Ce-based heavy fermions. *Rep. Prog. Phys.* **79**, 094503 (2016).
7. Das, D. *et al.* Magnetic field driven complex phase diagram of antiferromagnetic heavy-fermion superconductor $\text{Ce}_3\text{PtIn}_{11}$. *Sci. Rep.* **8**, 16703 (2018).
8. Kratochvíř M. *et al.* Coexistence of antiferromagnetism and superconductivity in heavy fermion cerium compound $\text{Ce}_3\text{PdIn}_{11}$. *Sci. Rep.* **5**, 15904 (2015).

9. Seyfarth, G. *et al.* Heavy fermion superconductor CeCu₂Si₂ under high pressure: Multiprobing the valence crossover. *Phys. Rev. B* **85**, 205105 (2012).
10. Wang, H. H. *et al.* Anomalous connection between antiferromagnetic and superconducting phases in the pressurized noncentrosymmetric heavy-fermion compound CeRhGe₃. *Phys. Rev. B* **99**, 024504 (2019).